Interaction physics of multi-picosecond Petawatt laser pulses with overdense plasma

A. J. Kemp, L. Divol

September 26, 2011

Physical Review Letters

Interaction physics of multi-picosecond Petawatt laser pulses with overdense plasma

A.J. Kemp and L. Divol
Lawrence Livermore National Laboratory, Livermore, CA
(Dated: September 23, 2011)

We study the interaction of multi-picosecond Petawatt laser pulses at relativistic intensities with overdense plasma using two- and three-dimensional kinetic particle simulations. We find that the ponderomotive force of the laser causes perturbations of the target surface leading to high absorption. We describe how non-linear saturation of these perturbations leads to emission of plasma from the target surface, thus stabilizing the surface, keeping absorption continuously high and creating three distinct groups of electrons with energies much greater than the usual ponderomotive scaling. We discuss the electron energy distribution and their divergence for applications like the fast-ignition approach to inertial confinement fusion.

PACS numbers: 52.57Kk, 52.65.Rr

The next generation of Petawatt short-pulse laser facilities like NIF-ARC, OMEGA-EP or FIREX-I will deliver up to 10 kilojoules of energy in focal spots with diameters of $40-100$ micrometers over several picoseconds at optical wavelengths [**?**]. Understanding the interaction physics of such pulses with solid targets is essential for basic high energy density science, and for applications like the fast-ignition approach to inertial confinement fusion (ICF), where such lasers could be used as drivers [1, 2].

Previous theoretical studies of relativistic laser plasma interaction have focused on sub-picosecond laser pulses with diffraction limited focal spots typically less than 10μm [3–7]. The interaction leads to the generation of 'hot' electrons with Boltzmann-like energy distributions peaking near the laser ponderomotive potential $k_B\,T_{\rm hot} = m_e c^2(\sqrt{1+a_0^2}-1)$ where $a_0 \equiv eE_0/m_e\,c\,\omega_L$ is the normalized laser field amplitude, resulting from stochastic acceleration of electrons in the laser electric and magnetic fields [3]. While fundamental absorption mechanisms and hot-electron production in short-pulse laser plasma interaction have been studied by many authors [**?**], a global picture of how these will interplay in realistic multi-picosecond Petawatt laser irradiation of dense plasma is still lacking.

This Letter addresses, for the first time, long-time evolution of the interaction of realistic Petawatt laser pulses with large spot diameters with over-dense plasma. We find that the ponderomotive force of the laser causes perturbations of the plasma interface leading to high absorption. We describe how non-linear saturation of these perturbations leads to emission of plasma from the target surface, thus stabilizing the surface, keeping absorption continuously high. Laser power is converted into a beam of energetic electrons that move, on average, in the laser direction. Within this beam we distinguish three groups of electrons with energies much greater than the usual $T_{\rm hot}$ scaling. We discuss the energy distribution within the electron beam and its divergence for applications like the fast-ignition approach to ICF.

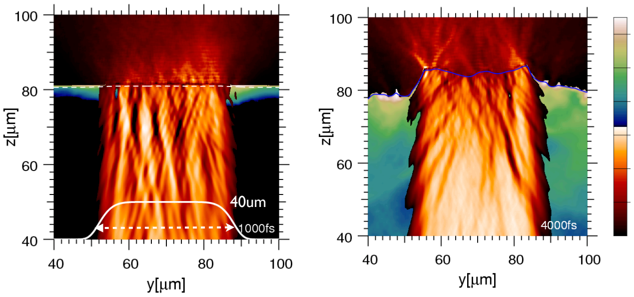

FIG. 1. Petawatt laser pulse interacting with over-dense plasma, (a) at 1 ps; and (b) at 4 ps. Laser Poynting flux and electron energy flux density along z (red); electron density below $10\,n_c$ (green); contour line of $10\,n_c$ in blue; transverse profile of input laser intensity (white).

The aim of this paper is to study the interaction of an energetic laser pulse with over-dense plasma over several ps at full scale through kinetic modeling in two- and three dimensional particle-in-cell simulations [8]. We set up a laser pulse with a transverse flat-top intensity profile $I(r,t) = I_0 \exp[-2(r/r_0)^8] \times \exp[-2((t-3\,t_0)/t_0)^2]$ where $I_0 = 1.37\times10^{20}\mathrm{W/cm}^2$, and a focal spot diameter $2\,r_0 = 40\mu$m, which is much larger than the diffraction-limited spots typically used in current experiments at comparable intensities [9]. This pulse contains ~ 10 kJ delivered to the target over 10 ps, consistent with fast-ignition requirements [2]; it is linearly polarized in the simulation plane with a wavelength $\lambda_L = 1\mu$m; rise time $t_0 = 200$ femtoseconds; for $t > 3\,t_0$, the time-dependent factor is set to one. We find that it is important to use a realistic rise time to avoid spurious effects. The plasma consists of deuterium ions and electrons at density $n_0 = 100\,n_c$, where critical density $n_c = \omega_L^2 m_e/4\pi e^2$. This is sufficient to guarantee $n_0 \gg a_0 n_c$, the density at which intense laser pulses are absorbed. After less than 1 picosecond, plasma expansion leads to a profile where the bulk density is not visible to the laser. The simulation box is $140\,\mu$m wide and $120\,\mu$m long, resolved with 50 cells per micron and 116 steps per laser period, using 120 electrons per cell; particles are initialized with a 0.1 keV thermal distribution. Boundary conditions are periodic in the transverse- and absorbing for particles and fields in the longitudinal direction.

Figure 1 illustrates the simulation set-up and early interaction at t=1 ps, i.e., about 1.2 ps after the laser has struck the target, and 3ps later. Small perturbations cause surface rippling driven by the ponderomotive force $F_z \sim B_x^2/l_s$, where B_x is the laser magnetic field amplitude on the plasma surface and $l_s = c/\omega_p \sim n_e^{-1/2}$ is the plasma skin depth. These ripples grow with time because plasma compression feeds back to an increased push F_z through a shortened skin depth l_s. The corresponding growth rate is of the order of femtoseconds, i.e., the laser period [10]. The present case is different from the gravitational Rayleigh-Taylor (RT) instability with a magnetic field parallel to the surface, where magnetic field tension acts to stabilize the surface [11]; it is not RT unstable in the classic sense, because acceleration and density gradient point in the same direction.

Rippling of the plasma surface is responsible for sustained high absorption because it prevents steepening of the plasma surface observed in 1D simulations [12]. Here, transverse gradients of the longitudinal electric field on the target surface induce perpendicular magnetic fields located at the side walls of filaments. These grow until the geometry of the electric field is locally radially symmetric, so that $|\nabla \times \mathbf{E}| << 1$. The resulting 'porous' structure of the laser-plasma interface, shown in Fig.2(a-c), allows ions to move from over-dense to under-dense regions and to replenish the under-dense plasma in front of the target with electrons. In contrast, 1D simulations predict an electrostatic sheath field near the point of absorption that is structured so that ions cannot escape the bulk plasma. This steepening leads to an artificial reduction in absorption over the course of about 1.5 ps under our laser and plasma conditions.

Non-linear saturation of the surface rippling sets in when a surface ripple grows to $\sim 1/2$ wavelength. Figure 2 presents a sequence of snapshots of the interaction region near 2.5 picoseconds. Images 2(a-c) show the ponderomotive pressure on the plasma surface which, together with the corresponding electrostatic field E_z, drops over a skin depth. When a surface ripple grows to a fraction of a wavelength, the ponderomotive force on its side wall drops, i.e., is 'shadowed', and plasma escapes in the transverse direction (y-axis), see Fig.2(b). Emitted electrons and ions are weakly magnetized in the emission's magnetic field of the order 100MG (ion velocity is about 0.01c, electron $\gamma = 20$) along the plasma surface. This field is frozen in the expanding plasma, so that a layer of plasma at a density near n_c forms near the surface over several microns. While plasma is advected away from the surface and density drops, the magnetic field is losing strength. At the end of the plasma emission (see Fig.2c), the ripple is 'deflated', leading to nonlinear saturation of the instability and an effective stabilization of the surface. As a consequence, the surface recedes without much pressure build-up in the dense plasma. Tracking the location where the laser is absorbed, we find that the surface moves at a near-constant rate $v_s \approx 5 \times 10^{-3} c$, compare Fig. 1. This velocity can be derived from momentum conservation between the impinging laser, plasma electrons and bulk ions [3]. In our case, a large fraction of laser momentum $f_a \approx 0.7 - 0.8$ is absorbed into relativistic electrons, different from Ref. [3], while $1 - f_a$ is reflected, so the fraction of momentum transferred to bulk ions is $2(1 - f_a)$. Hence, the momentum balance between the laser pulse $I_L/c \equiv a_0^2\, m_e\, c^2/2$ and that absorbed in the plasma writes $(1 - f_a)\, a_0^2 n_c m_e c^2 = 2 M_i\, n_i\, v_s^2$, where n_i is the bulk ion density.

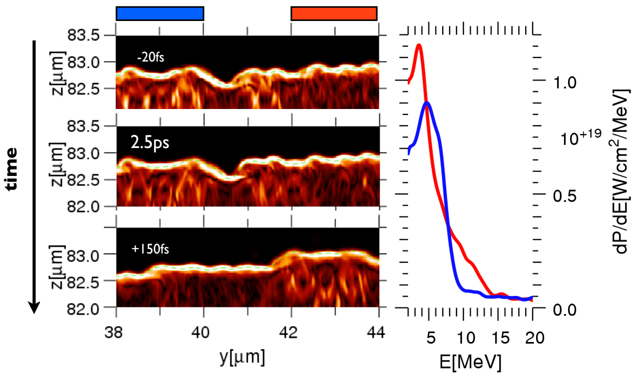

FIG. 2. Surface emission of electrons; (a-c) snapshots of ponderomotive force $|\nabla(<\mathbf{E}^2 + \mathbf{B}^2>)/2|$; blue and red boxes indicate where spectra are taken; (d) energy spectra in left/right box indicated on top of (a).

We now discuss how non-linear saturation of the surface rippling leads to the generation of three groups of fast electrons via distinct absorption mechanisms.

(1) For a clean plasma density step the interaction is dominated by particles that originate in the over-dense plasma region. Particles which, by means of their thermal velocities in the bulk plasma, enter the vacuum region, get accelerated in the standing-wave pattern of the laser electro-magnetic fields in front of the surface. Their excursion length is a fraction of a laser wavelength before they are pushed back into the target where they cease to interact with the laser; as a result, their energy is limited by the ponderomotive energy; the resulting energy spectrum has a cut-off near $1.5\, E_p \sim 7\,\mathrm{MeV}$ for $a_0 = 10$ [12, 13]. The resulting energy spectrum is shown by the blue curve in Fig. 2(d) which represents a region with no recent electron emission. Figure 3 discusses the evolution of electron energy spectra determined 3μm behind the laser interaction region and corresponding density profiles in the laser spot region. By 2 ps the steep

part of the density profile, where the first group of electrons is generated, assumes a scale length of $l_p = 0.15\mu$m between n_c and $10\,n_c$ where laser is absorbed. This scale is given by the Debye length for density $a_0\,n_c$ and temperature $a_0\,m_e c^2$, giving $l_p = \sqrt{a_0\,m_e c^2/(4\pi e^2 a_0 n_c)}$, which we confirmed by separate 2D simulations at various intensities and initial plasma gradient lengths. The scale length l_p is independent of laser intensity and initial conditions of the plasma, but depends on laser wavelength alone. Emission of plasma from the target surface modifies this idealized scenario in that 100 MG magnetic fields generated by surface currents deflect electrons with sub-ponderomotive energies, so that the net electron energy flux behind the plasma surface drops locally.

(2) Laser interaction with the plasma emitted by deflating surface ripples, which extends as a density plateau just below n_c over several microns from the surface as shown in Fig.3(b), accelerates particles to energies beyond the ponderomotive potential, giving rise to a second group of electrons. This is shown in more detail in Fig.2d, where we compare an energy spectrum immediately behind the plasma emission (red curve) to one at a location with no recent emission (blue curve). On average, the plasma emission gives rise to a hotter spectrum than expected from a density step alone, because the distance over which electrons interact with the laser is extended compared to the clean interface [14].

(3) After a few picoseconds, the emission of particles from the target surface leads to filling of the vacuum region in front of the target with under-dense plasma. Laser acceleration in this plasma gives rise to a third group of electrons with energies up to 150 MeV in the case considered here. The density profile flattens with time and reaches a scale length of $\sim 50\mu$m in which electrons are accelerated via an inverse free-electron laser mechanism, giving a Boltzmann-like spectrum with a slope $T_{\rm eff} = 1.5 \times (I_{\rm laser}/10^{18}\,{\rm W/cm^2})^{1/2} \approx 17.5\,$MeV, which is much greater than expected from ponderomotive scaling [14]. The density profile resembles an isothermal rarefaction $n_e(z,t) = n_{e,0}\,\exp(-z/c_s t)$ with a sound velocity $c_s = \sqrt{(Z\,m_e c^2/A\,m_p)\,a_0}$ and an electron temperature $a_0\,m_e c^2$ determined by the laser amplitude. Over a wide range of laser intensities we find $n_{e,0} \simeq 0.15\,n_c\,a_0^{1/2}$, with the pre-factor determined by details of the surface emission. The power driving such an isothermal rarefaction $4(A/Z)m_p\,n_{e,0}\,c_s^3$ amounts to only $\sim 1\%$ of the incident laser power [15]. Due to the finite laser spot size, the expansion remains one-dimensional until its scale length exceeds the spot diameter, here at $\sim 4\,$ps, which explains the asymptotic scale length of under-dense plasma observed in our simulation.

We have verified the distinction between these groups and the characterization of their histories by tracking test particles in our simulation. Note that an unrealistic ion mass or a transverse simulation box width less than ten wavelengths, in which the number of spatial surface modes is limited, will lead to an under-estimation of the surface emission effect. Another important assumption made above is that the plasma kinetics depends only on the ratio of ion charge and mass Z/A and not on A separately, which means that the time scales found here can be generalized to any fully plasma. We have verified that this is the case in separate simulations.

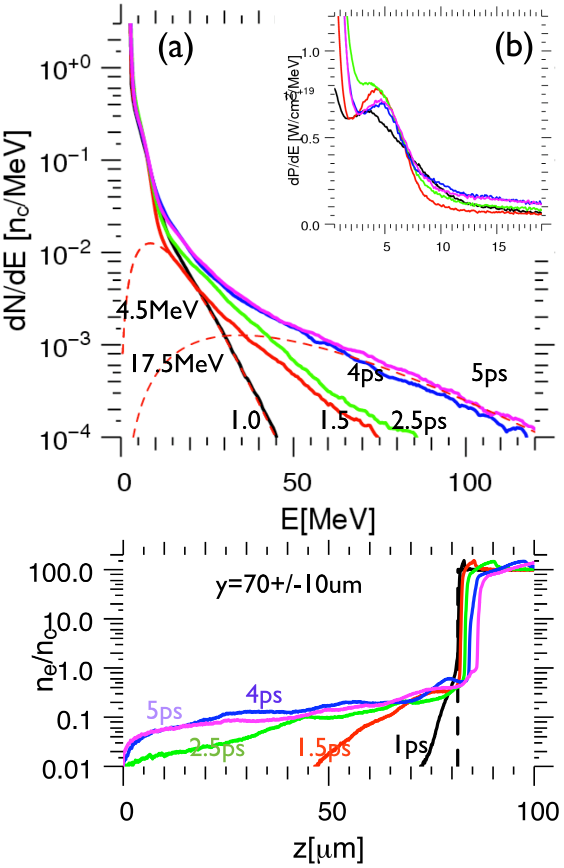

FIG. 3. (a) Electron energy spectra and (b) electron density profiles in the laser spot, for several times during the interaction. Initial density profile and relativistic Maxwellian fits to electron spectra are indicated by dashed lines as labeled.

For applications of Petawatt lasers like fast-ignition ICF, we discuss the energy distribution of the electron beam as a function of time and its divergence more quantitatively. Figure 4 shows the partition of energy flux P_z along the laser direction between absorbed light and the laser-generated electron beam as determined behind the absorption interface via

$$\mathbf{P}_{\rm el} = P_0\,L_y\,N_z^{-1}\,n_i \sum_n \mathbf{v_n}(\gamma_n - 1)w_n \qquad (1)$$

over a $3\,\mu$m deep volume across the simulation box, with $P_0 \equiv m_e c^3 n_c = 2.74 \times 10^{18}{\rm W/cm^2}$ and $N_z = 150$ the

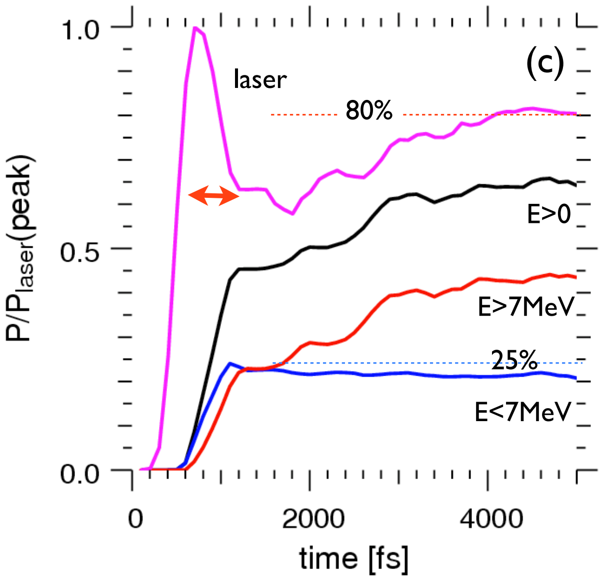

FIG. 4. Time-history of energy partition in laser generated electron flux; (a) energy spectra for five time steps and relativistic Maxwellian distributions with $T = 4.5$ and 17.5MeV; (b) energy flux spectra near $E_p = 4.5$ MeV; (c) longitudinal components of net Poynting flux at $z = 0$, electron energy flux at $z = 90\,\mu$m, and contributions by particles with $E < 7$ MeV and $E > 7$ mEV; values normalized to peak injected laser flux. Arrow indicates time lag due to distance between laser injection and target surface

number of cells along z over which is averaged. On top we show the net laser energy flux through the injection plane at $z = 0$. It peaks at ~ 0.7 ps before reflected light reaches the injection plane. The time lag between laser and electron flux is due to the finite distance between injection plane and target surface. At $t = 1$ ps the fraction of energy coupled into the first group of 'ponderomotive' electrons is $\sim 25\%$ of the laser power; this value drops with time due to pump depletion of the laser in expanding plasma. Absorption into super-ponderomotive energies rises from 15% at 1 ps to nearly 45% of peak power as the region in front of the target fills with under-dense plasma. At 4 ps, the scale length of the under-dense plasma reaches $\sim 50\mu$m; the energetic tail up to 150 MeV is generated by laser plasma interaction in under-dense plasma. From the net Poynting flux in the injection plane, shown in Fig. 4, we find that around 80% of the laser energy are absorbed. The difference between the electron flux along z and the net laser flux can be explained by the divergent nature of the electron beam. Assuming the beam is symmetric, we get a mean divergence angle of $\pm 35°$ averaged across the simulation box in 2D. This value is consistent with an alternative measure of beam divergence as a Gaussian distribution of energy flux density with respect to angle, determined in the same 3μm deep box behind the laser spot in over-dense plasma as the one used above.

Comparing the reference case shown above to a three-dimensional simulation for a laser spot that is scaled down by 1/2 in a smaller box with similar target conditions, we find that 2D results (for laser polarization in the simulation plane) are essentially a central cut through an equivalent 3D run. However, an important feature observed only in three-dimensional simulations is the isotropization of the forward moving electrons in the plane perpendicular to the laser propagation axis. In 2D cartesian simulations, particles cannot gain momentum perpendicular to the simulation plane for symmetry reasons.

In conclusion, we have studied the interaction of realistic Petawatt laser pulses with over-dense plasma for several picoseconds using large scale kinetic particle in cell simulations in 2D and 3D, to extrapolate by an order of magnitude beyond what is experimentally accessible today in terms of laser energy. We find that after a few picoseconds more than 80% of the laser light are absorbed into electrons that are more energetic than suggested by ponderomotive scaling. Perturbations of the target surface driven by light pressure lead to the emission of plasma into the vacuum region in front of the target. Emission of plasma from the surface enhances the absorption into super-ponderomotive electrons to levels comparable to cases that started out with preformed plasma, i.e., the interaction becomes largely independent of initial plasma conditions; leads to non-linear saturation of the perturbations; and, in turn, is responsible for continuously high absorption. Steady absorption into electrons around the ponderomotive energy at a 25% level has important implications for fast ignition, where MeV electrons deposit their kinetic energy to the dense core of a compressed DT pellet. Due to the expected density-length product of around 2 g/cm^2 only electrons within an energy range of 1-3 MeV will contribute significantly to core heating.

We thank M. Tabak, B. Cohen, M. Key, Y.Sentoku, D. Strozzi,and P. Patel for helpful discussions and encouragement. This work was supported by the Office of Fusion Energy Sciences. Simulations were carried out on the Livermore Computing Center's Sierra cluster under a Grand Challenge allocation. This work was performed under the auspices of the U.S. Department of Energy by the Lawrence Livermore National Laboratory under Contract DE-AC52-07NA27344.

---

[1] M. Tabak *et al.*, Phys Plasmas **1**, 1626 (1994).
[2] S. Atzeni and M. Tabak, Plasma Physics and Controlled Fusion **47**, B769 (2005).

[3] S. C. Wilks, W. Kruer, M. Tabak, and A. B. Langdon, Phys Rev Lett **69**, 1383 (1992).

[4] J. Adam, A. Héron, and G. Laval, Phys Rev Lett **97**, 205006 (2006).

[5] B. Chrisman, Y. Sentoku, and A. J. Kemp, Phys Plasmas **15**, 056309 (2008).

[6] J. Tonge *et al.*, Phys Plasmas **16**, 056311 (2009).

[7] B. F. Lasinski *et al.*, Phys. Plasmas **16**, 012705 (2009).

[8] H. Ruhl, *in: Introduction to Computational Methods in Many Body Physics* (Rinton Press, Paramus, NJ, 2006).

[9] A. G. Macphee *et al.*, Phys Rev Lett **104**, 55002 (2010).

[10] E. G. Gamaly, Physical Review E **48**, 2924 (1993).

[11] S. Chandrasekhar, *Hydrodynamic and Hydromagnetic Stability* (Courier Dover, Oxford, UK, 1961).

[12] A. Kemp, Y. Sentoku, and M. Tabak, Physical Review E **79**, 66406 (2009).

[13] J. May *et al.*, Physical Review E **84**, 025401 (2011).

[14] A. Pukhov and J. M. ter Vehn, Phys Rev Lett **76**, 3975 (1996).

[15] S. Atzeni and J. Meyer-ter-Vehn, *The physics of inertial fusion* (Oxford University Press, Oxford, UK, 2004).